Journal of
Composites Science

MDPI

Article

Influence of Solid-Phase and Melt-Quenching $Na_3Fe_2(PO_4)_3$ Polycrystal Production Technology on Their Structure and Ionic Conductivity

A. S. Nogai [1], A. A. Nogai [1,*], D. E. Uskenbaev [1], E. A. Nogai [1], A. B. Utegulov [1], P. A. Dunayev [1], A. S. Tolegenova [1], Bazarbek Assyl-Dastan Bazarbekuly [2,*] and A. A. Abikenova [1]

[1] Department of Radio Engineering, Electronics and Telecommunications, S. Seifullin Kazakh Agrotechnical Research University, Astana 010000, Kazakhstan; nogay06@mail.ru (A.S.N.)
[2] Department of Space Technique and Technology, L.N. Gumilyov Eurasian National University, Astana 010000, Kazakhstan
* Correspondence: artur.n00@mail.ru (A.A.N.); asyl.bazarbek.92@mail.ru (B.A.-D.B.)

Abstract: This article studies the influence of solid-phase (type 1 samples) and melt-quenching (type 2 samples) technological modes of obtaining $Na_3Fe_2(PO_4)_3$ polycrystals on their structures and ion-conducting properties. α-$Na_3Fe_2(PO_4)_3$ polycrystals of the 1st type are formed predominantly under an isothermal firing regime, and the synthesis of the 2nd type is carried out under sharp temperature gradient conditions, contributing to the formation of glassy precursors possessing a reactive and deformed structure, in which the crystallization of crystallites occurs faster than in precursors obtained under isothermal firing. The elemental composition of α-$Na_3Fe_2(PO_4)_3$ type 2 polycrystals is maintained within the normal range despite the sharp non-equilibrium thermodynamic conditions of synthesis. The microstructure of the type 1 $Na_3Fe_2(PO_4)_3$ polycrystals is dominated by chaotically arranged crystallites of medium (7–10 μm) and large (15–35 μm) sizes, while the polycrystals of type 2 are characterized by the preferential formation of small (3–4 μm) and medium (7–10 μm) crystallites, causing uniaxial deformations in their structure, which contribute to a partial increase in their symmetry. The advantage of type 2 polycrystals is that they have higher density and conductivity and are synthesized faster than type 1 samples by a factor of 4. The article also considers the issues of crystallization in a solid-phase precursor from the classical point of view, i.e., the process of the formation of small solid-phase nuclei in the metastable phase and their growth to large particles due to association with small crystallites using phase transitions. Possible variants and models of crystallite growth in $Na_3Fe_2(PO_4)_3$ polycrystals, as well as distinctive features of crystallization between two types of samples, are discussed.

Keywords: polycrystals; melt-quenching of synthesis; glass-phase precursors; crystallite growth; structural parameters; ion-conducting properties

Citation: Nogai, A.S.; Nogai, A.A.; Uskenbaev, D.E.; Nogai, E.A.; Utegulov, A.B.; Dunayev, P.A.; Tolegenova, A.S.; Bazarbekuly, B.A.-D.; Abikenova, A.A. Influence of Solid-Phase and Melt-Quenching $Na_3Fe_2(PO_4)_3$ Polycrystal Production Technology on Their Structure and Ionic Conductivity. *J. Compos. Sci.* **2024**, *8*, 354. https://doi.org/10.3390/jcs8090354

Academic Editor: Chun-Liang Yeh

Received: 27 June 2024
Revised: 31 August 2024
Accepted: 3 September 2024
Published: 9 September 2024

1. Introduction

The development of energy storage technology and renewable energy sources is urgent [1–3]. Lithium-ion batteries (LIBs) are leaders among other types of batteries, but there are still problems with their recycling after decommissioning [3]. Therefore, there are problems with reusing obsolete LIBs. In addition, frequent fires and explosions occur during the operation of LIBs, which limits their widespread use [4]. In addition, the high cost of lithium and LIBs makes it necessary to search for cheaper sodium-ion batteries (SIBs) [5]. SIBs require sodium-containing materials, which are more common, safer in operation, and cheaper in cost than lithium and lithium compounds [6]. Considering that many materials are required for large-scale high-energy rechargeable batteries, it is reasonable to fabricate electrode materials from cheap and common elements. For example,

for the electrodes of large-scale rechargeable sodium batteries, iron and manganese can be such materials [7].

The interest in phosphate-based cathode materials for use in SIBs is due to the variety of their structures, their good structural stability, their ability to provide sodium cations with high mobility, and their operational safety [8]. Among the NASICON (Natrium Super Ionic CONduction) phosphate compounds, orthophosphates are the most attractive. The anionic sublattice of sodium-containing orthophosphates of the NASICON family is constructed by joining MO_6 and RO_4polyhedra. In this case, cavities M(1) and M(2) are formed in the crystal framework, due to which three-dimensional "conduction channels" for the movement of sodium cations are formed [9,10]. Information about the crystal structure of NASICON-type samples with the cationic positions M(l) and M(2) for the placement of sodium cations is given in [11,12]. Among the samples from the NASICON family, the structure and conductivity of $Na_3Sc_2(PO_4)_3$ mono- and polycrystals have been established, and their anisotropic properties, i.e., the dependence of ion transport on the orientation of $Na_3Sc_2(PO_4)_3$ single crystals, have been clarified [12–16]. Their isostructural analog is $Na_3Fe_2(PO_4)_3$, which could be used as a cathode for SIB since it possesses a theoretical electrical capacity of 105 mAh g^{-1}.

The structure of low-symmetric phase α-$Na_3Fe_2(PO_4)_3$ is superstructural and monoclinic-distorted, and is characterized by the dipole ordering of the antiferroelectric (AFE) type [17,18]. The parameters of the superstructural unit cell of single-crystal α-$Na_3Fe_2(PO_4)_3$ can be represented by the following expressions [19].

$$\vec{a} = \vec{a_1}; \vec{b} = \vec{b_1}; \vec{c} = \vec{a_1} + 3\vec{c_1}, \quad (1)$$

where the parameters of the monoclinic cell are as follows: a_1 = 15.127(3) Å; b_1 = 8.722(2) Å; c_1 = 8.793(1) Å.

After the α→β phase transition, the structure of single-crystal β-$Na_3Fe_2(PO_4)_3$ becomes rhombohedral (pr. gr. R3c), but with weak superstructural reflexes; this can be written as follows [19]:

$$\vec{a_\beta} = 2\vec{a_1}; \vec{b_\beta} = 2\vec{b_1}; \vec{c_\beta} = \vec{c_\gamma}, \quad (2)$$

The structural parameters of rhombohedral-phase γ-$Na_3Fe_2(PO_4)_3$ were established earlier and have the following values: a = 8.733 Å, c = 21.798 Å [20]. Also, the conductivity in different polymorphic phases was studied in [17,19–21]. For example, γ-$Na_3Fe_2(PO_4)_3$ is in the superionic state after the two phase transitions α→β and β→γ [17], since its highly symmetric crystal structure has "open conduction channels" along three crystallographic directions. In addition, the structural changes in the anionic and cationic parts of the crystal framework during phase transitions in $Na_3Fe_2(PO_4)_3$ were studied using DTA, Meissbauer, and impedance spectroscopy methods in [22].

The advantage of $Na_3Fe_2(PO_4)_3$ is the stability and flexibility of the crystal structure due to the mobility of the PO_4 groupings that form the basis of its anionic crystalline framework [23]. However, the disadvantage of this material is that the $Na_3Fe_2(PO_4)_3$ polycrystal synthesized by the solid-phase method when used as a cathode in SIB has a small reversible discharge capacity of 61 mAh g^{-1} at a potential of 3.5 V [24]. The reason for this is that α-$Na_3Fe_2(PO_4)_3$ has low ionic and electronic conductivity because it is a dielectric in the α-phase. The ionic conductivity of α-$Na_3Fe_2(PO_4)_3$ can be enhanced by modifying the structure [17,25,26], and the electronic conductivity can be enhanced by introducing carbon materials into its composition [27–29].

The relationship between the structures, properties, and grain growth of polycrystals was studied in [30–33]. The behavior of grain growth during firing strongly influences the microstructure formation of polycrystalline materials [34]. Many crystal growth mechanisms are usually described by grain growth behaviors [35,36]. Classical theories of grain growth in monophase polycrystalline materials are given in [37]. No isothermal issues related to the grain growth in metals and alloys are considered in [38]. So far, there is no unified and clear theory regarding solid-phase crystallization, so the collection and

analysis of empirical data on crystallite growth in polycrystals of different classes using different methods of polycrystal synthesis are relevant. Based on the above, it follows that it is relevant to investigate the effect of different α-$Na_3Fe_2(PO_4)_3$ polycrystal synthesis methods on their structures and conductive properties. For example, the influence of using melt-quenching to obtain $Na_3Fe_2(PO_4)_3$ polycrystals on their structure and ion-conducting properties has not been studied. This method invovles melting the initial reactants under the influence of infrared radiation (IR) and then cooling them sharply to obtain glassy precursors. Next, a polycrystal should be obtained by firing mechanically crushed and pressed glassy precursors.

To evaluate the advantages of using melt-quenching to perform synthesis, a comparative study of the influence of using the solid-phase and melt-quenching methods of producing $Na_3Fe_2(PO_4)_3$ polycrystals on their structure and ion-conducting properties was carried out.

2. Materials and Methods

2.1. Synthesis of Samples

Polycrystalline $Na_3Fe_2(PO_4)_3$ samples were synthesized by conventional ceramic technology and the melt-hardening method. The starting reagents were oxides, salts of sodium carbonate, and ammonium phosphate: Na_2CO_3, Fe_2O_3, and $NH_4H_2PO_4$ of "Ch. D.A." grade.

The stoichiometric compositions of the Na_2CO_3, Fe_2O_3, and $NH_4H_2PO_4$ reagents (mechanically ground in a planetary mill, with the mixture then was pressed into tablets) were pre-annealed for 2 h at a temperature of 350 °C. The reagent tablet obtained after annealing was subjected to grinding and the mixture was pressed into tablets.

Type 1 polycrystals were prepared by two-fold firing in a muffle furnace in the air at 600 °C and at 800 °C with additional homogenizing grindings. After the first stage of roasting the amorphous phases of $Na_3Fe_2(PO_4)_3$ at 600 °C for 7 h, type 1 precursors were obtained. The $Na_3Fe_2(PO_4)_3$ type 1 polycrystals were obtained by firing the secondary isothermal precursors for 7 h and decreasing the temperature from 800 °C to 750 °C (in 1 h).

The preparation of the $Na_3Fe_2(PO_4)_3$ type 2 polycrystals by melt-quenching was carried out in two steps. First, glassy precursors were obtained by melting the mixture of reagents at 950 °C under the action of heat and the infrared radiation (IR) energy of the heating elements in the furnace (samples were loaded into the stove on a platinum stand, i.e., without crucible method), and by its sharp cooling or quenching of the melt. Melt-quenching was carried out by dropping it from the furnace onto the cooled walls of the quenching device. At the second stage, the glassy precursors were milled, pressed into tablets, and isothermally fired in a muffle furnace at 800 °C for 2 h. The synthesis modes used for the polycrystalline samples are given in Table 1.

Table 1. Technological modes of the synthesis of polycrystalline samples of $Na_3Fe_2(PO_4)_3$, types 1 and 2.

Samples	**Type 1**		**Type 2**	
$Na_3Fe_2(PO_4)_3$	**1st Annealing**	**2nd Annealing**	**1st Annealing**	**2nd Annealing**
Firing temperatures T, °C	600	800	950	800
Firing time t_F, h	7	7	0.013	2
Cooling time t_C, h		1	0.083	1
Temperature cooling rate v, °C/h		48	11,445.78	48

Table 1 shows that the preparation of type 1 polycrystals was carried out under the isothermal regime, while the preparation of the precursors for the type 2 samples was

carried out under the non-equilibrium regime with a sharply gradient temperature. In addition, the preparation of the polycrystals differs both in methodology and synthesis modes.

2.2. Polycrystal Studies

The structures of the $Na_3Fe_2(PO_4)_3$ samples were investigated by powder X-ray diffraction methods, using the Bruker D8 ADVANCE diffractometer (Karisruhe, Germany) (CuK_α—radiation) and the Hitachi TM3030 scanning electron microscope (Hitachi High-Tech, Tokyo, Japan) with a Bruker microanalysis system. The crystallite sizes were determined from the microstructure of polycrystals by using the "Image J" User program v 1.54h. This program allows the area of crystallites to be determined from the pixels reflected from the microstructure image; then, the radius r of the crystallites can be determined (crystallites are considered as a material point with radius r). The density of the prepared polycrystals was studied using the psychometric method.

The conductive properties of the polycrystalline samples were measured by the impedance method using an LCR 8101G device (Kuala Lumpur, Malaysia). A silver electrode was used as a blocking electrode (the silver electrode remained on the samples after the application and burning of the silver paste).

3. Results of the Study and Their Discussion

3.1. Structural Data of $Na_3Fe_2(PO_4)_3$ Polycrystals

$Na_3Fe_2(PO_4)_3$ polycrystals with a dark brown color were prepared and were in the form of tablets (10 mm diameter and 1 mm thickness). After the preliminary calcination of the mixture of starting reagents at 350 °C for 2 h, amorphous phases of $Na_3Fe_2(PO_4)_3$ were obtained, as no peaks were detected in the diffractogram (Figure 1a). These amorphous phases were used to obtain $Na_3Fe_2(PO_4)_3$ precursors of types 1 and 2.

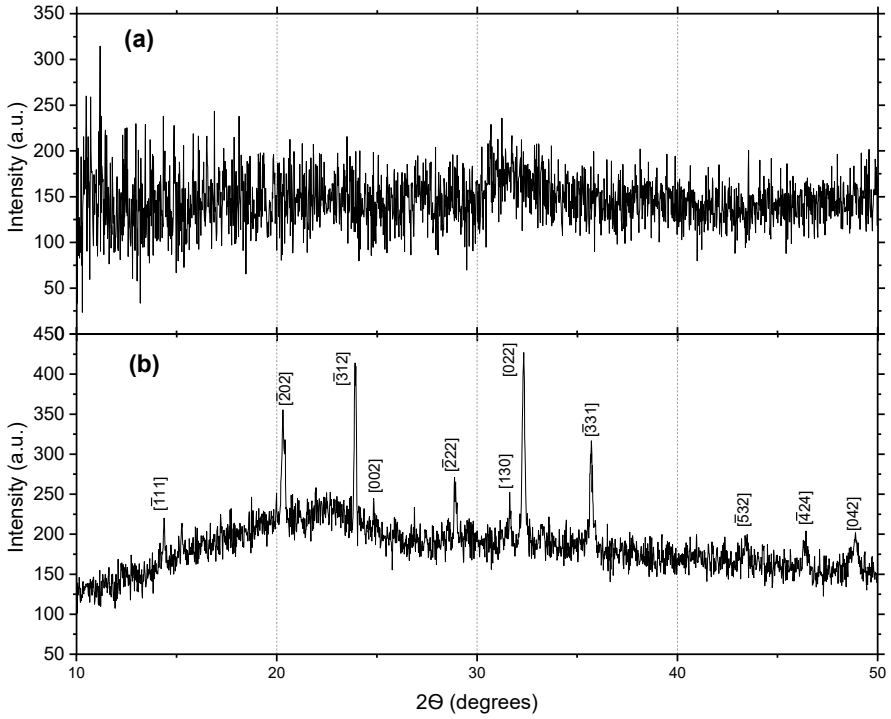

Figure 1. X-ray diffractograms of (**a**) amorphous phases of $Na_3Fe_2(PO_4)_3$ (after firing at 350 °C for 2 h) and (**b**) type 1 amorphous–crystalline precursors (after one firing at 600 °C for 7 h) (The designations of the crystallographic planes [hkl] are given on the diffraction peaks).

After the first step of roasting the amorphous phases of $Na_3Fe_2(PO_4)_3$ at 600 °C for 7 h, amorphous–crystalline precursors of type 1 samples were formed, the diffractograms of which are shown in Figure 1b.

Thus, the formation of type 1 amorphous–crystalline precursors occur only after the pro-longed isothermal firing of amorphous $Na_3Fe_2(PO_4)_3$ phases (at 600 °C for 7 h).

Type 2 precursors were obtained by the melt-quenching of amorphous $Na_3Fe_2(PO_4)_3$ phases (see Table 1). In this process, thin and thick solidified precursors were obtained, so the diffractograms of each of them were taken separately. Figure 2 shows X-ray diffractograms of the type 2 precursors obtained: (a) from thin plates; (b) from thick plates.

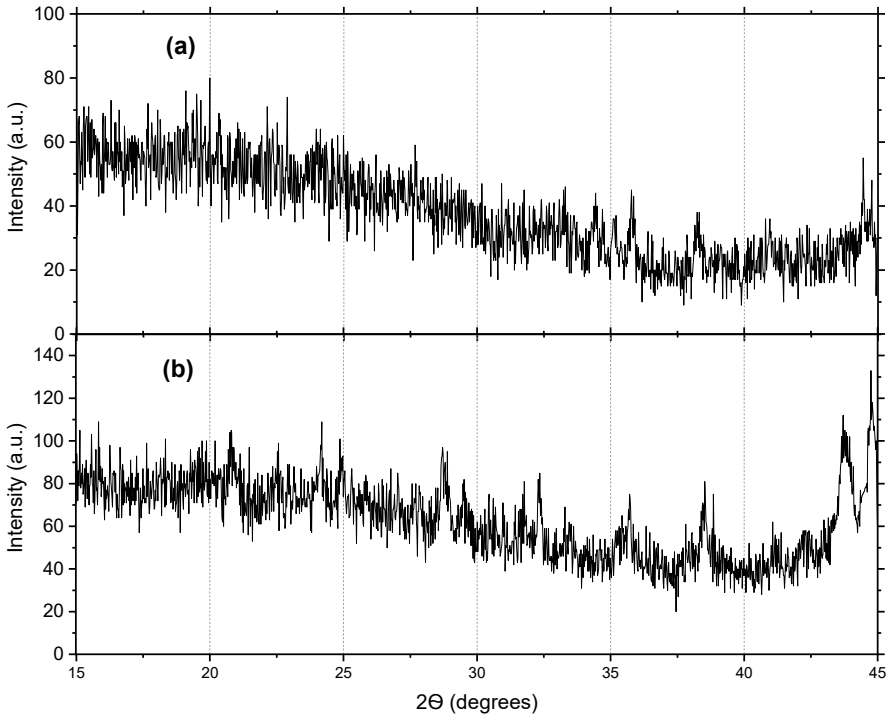

Figure 2. X-ray diffractograms of type 2 glassy precursors prepared by melting amorphous phases of $Na_3Fe_2(PO_4)_3$ at 950 °C and cooling the melt: (**a**) from thin plates; (**b**) thick plates.

Judging from the diffractogram in Figure 2a, the glassy precursor of the thin plate (small particles) is amorphous (no peaks) as its cooling is rapid. In Figure 2b, the glassy precursor thick plate is amorphous–crystalline, as its cooling is slower than the thin plate, and individual peaks of the crystalline phase have time to appear in the diffractogram. Since type 2 polycrystals are obtained by firing a mixture of glassy precursors of thin and thick plates, these precursors can be considered as amorphous–crystalline.

Figure 3 shows the diffractograms of $Na_3Fe_2(PO_4)_3$ polycrystal powders prepared by solid-phase synthesis, samples of type 1; and by melt-quenching, samples of type 2.

It was found that $Na_3Fe_2(PO_4)_3$ polycrystals of both types have a monoclinic distorted syngony of space group C2/mThe type 2 polycrystals crystallized better as they had more intense peaks than the type 1 samples (see Figure 1). The angles and peaks of the experimental diffractogram corresponding to the main phase of α-$Na_3Fe_2(PO_4)_3$ were identified using the CELREF program with data in the literature about space groups and the cell parameters of sodium ferric orthophosphate [19,20].

The diffractograms of the samples were identified using the“CELREF” program and the calculated data are given in Table 2.

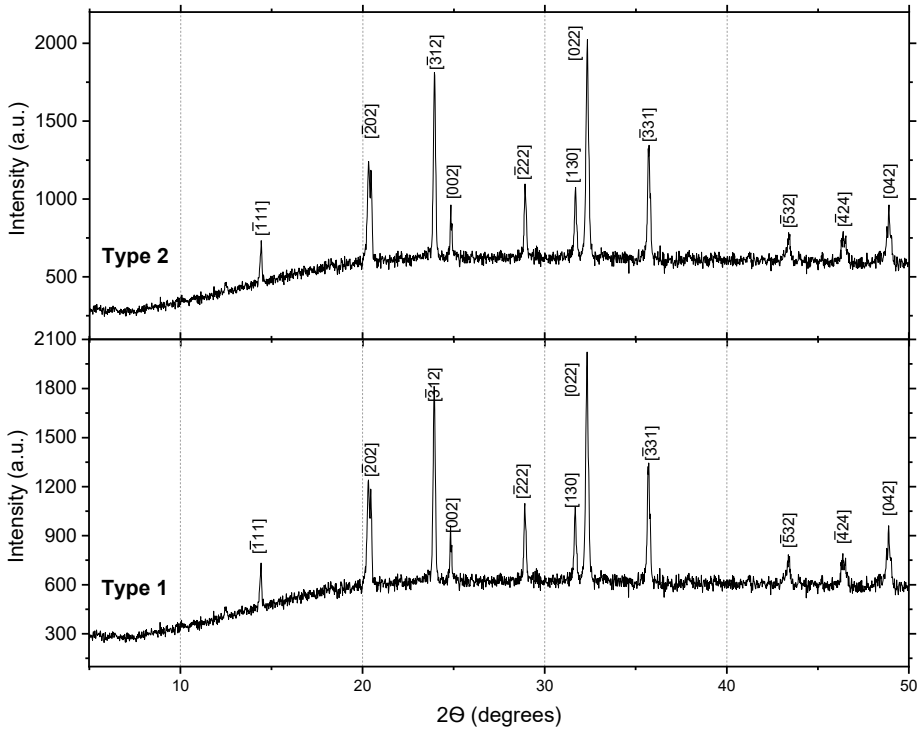

Figure 3. X-ray diffractogram of $Na_3Fe_2(PO_4)_3$ polycrystals: type 1 and type 2.

Table 2. Unit cell parameters of $Na_3Fe_2(PO_4)_3$ polycrystals.

Compound $Na_3Fe_2(PO_4)_3$	Space Group	Unit Cell Parameters						Ref.
Types of Samples		**a, Å**	**b, Å**	**c, Å**	**α^0**	**β^0**	**γ^0**	
Polycrystal 1st Type.	C2/m	15.1230	8.7168	21.5963	90.0	90.33	90.0	
		Δ = 0.0214	Δ = −0.028	Δ = −0.0195	0	Δ = 0.03		
Polycrystal 2-nd Type	C2/m	15.1444	8.6840	21.5768	90.0	90.30	90.0	
Standard values of structural parameters	C2/m	15.346	8.744	21.644	90.00	90.03	90.00	[24].

The unit cell data of the polycrystals shown in Table 2 show the differences between the samples of types 1 and 2 (the difference between the parameters is indicated by Δ). Also, for comparison, Table 2 shows the standard values of the structural parameters of $Na_3Fe_2(PO_4)_3$, which was also synthesized by the solid-phase method but at lower temperatures (at 600 °C for 10 h) than the polycrystals of types 1 and 2; this is because more reactive initial reagents were used as reagents [20]. Since the structure of the standard samples of α-$Na_3Fe_2(PO_4)_3$ was subjected to minimum temperature influence during its synthesis, they can be taken as a reference.

The table shows that there is a marked increase in the unit cell parameter, Δa = 0.2014 Å, and a decrease in the parameters Δb = −0.028 Å and Δc = −0.0195 Å for the type 2 samples relative to the type 1 samples. At the same time, the angle β of the type 2 polycrystal was reduced by Δβ = 0.030°, relative to the type 1 sample. The noted changes in the structural parameters of the type 2 polycrystal relative to the type 1 sample could be related to the uniaxial deformations created in the sample due to the synthesis conditions having a sharp temperature gradient.

The density of the type 1 $Na_3Fe_2(PO_4)_3$ polycrystal samples was 81% of the theoretical one, and for the type 2 samples, the density reached 96%.

Probably due to the heat treatment of both types of samples at higher temperatures, differences in the parameters between the indicated α-$Na_3Fe_2(PO_4)_3$ polycrystals and the standard sample are observed (see Table 2).

3.2. Crystallizations Results of $Na_3Fe_2(PO_4)_3$ Polycrystals

The microstructures of the α- $Na_3Fe_2(PO_4)_3$ polycrystals of types 1 and 2 are shown in Figure 4.

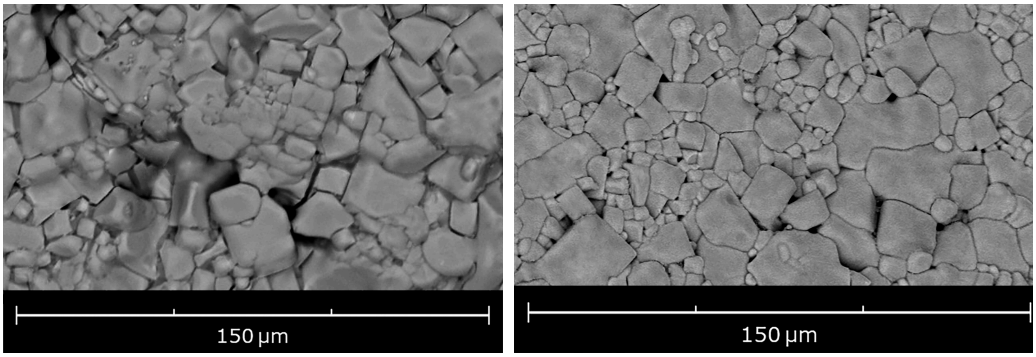

Figure 4. Microstructures of α-$Na_3Fe_2(PO_4)_3$ polycrystals of type 1 (**a**) and type 2 (**b**).

The microstructures of the type 1 polycrystals (see Figure 4a) were formed under a regime of prolonged isothermal firing and short-term cooling (8 h).

On the contrary, for the type 2 samples, the crystallization period was short-term, i.e., the duration of isothermal annealing (2 h) and cooling (1 h) was only 3 h. Both types of samples are characterized by the presence of large (15–35 µm), medium (7–10 µm) and small (3–4 µm) crystallites in polycrystals. However, from the graph presented in Figure 5, the proportion of small crystallites in the type 2 polycrystal is much larger than that of the type 1 samples.

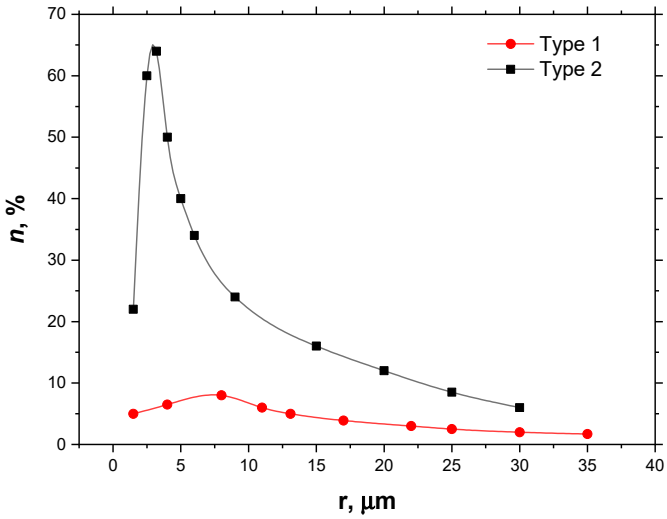

Figure 5. Dependence of the fraction of crystallites on their sizes in α-$Na_3Fe_2(PO_4)_3$ polycrystals: for type 1 samples and for type 2 samples.

Obviously, it relates to a small period of crystallization in samples of type 2. Nevertheless, the appearance of medium and large crystallites can be associated with the intensive absorption of small particles by large particles. On the contrary, in samples of type 1, the share of medium crystallites from their total number prevails (see Figure 5).

The reason for this difference in the synthesis time is the significant differences in the methods of obtaining and the modes of preparing the precursors. The precursors for the samples of type 2 are prepared in a short period of time and under sharper temperature gradient conditions of melting and cooling (see Table 1).

Solid-phase crystallization from an amorphous solid phase consisting of dispersed particles can be regarded as a homogeneous process. Crystallization will occur via the formation of small solid-phase nuclei (in a limited space) and their growth (towards larger particles) due to their association with small crystallites through phase transitions (FTs). It is likely that amorphous–crystalline precursors of type 1 are obtained by the isothermal firing (T = 600 °C) of amorphous phases of $Na_3Fe_2(PO_4)_3$ (Figure 1a), when particles of the substance pass into a metastable state with Gibbs energy (G_{MS}). Also, in the metastable phase, the appearance of crystallite germs with Gibbs energy (G_{Snk}) is possible because of fluctuation processes. Moreover, the transition from the metastable phase to the crystallite phase is possible only by phase transitions (PT) ($G_{MS} \rightarrow G_{Snk}$) at temperature T_c. According to Gibbs theory, such a transition is possible if there is a loss of free energy in the substance, i.e., $\Delta G_{MS} < 0$. Figure 6 schematically shows the possible crystallization processes: (a) from liquid phase (L) to solid phase [35] and (b) from metastable phase (ΔG_{MS}) to solid phase after temperatures T_c of FT. The intersecting dashed line (G_{ms}) with the line (G_s) at the point G_{snk} indicates that the particle of the metastable phase (circle) transitions to the solid phase (Figure 6b).

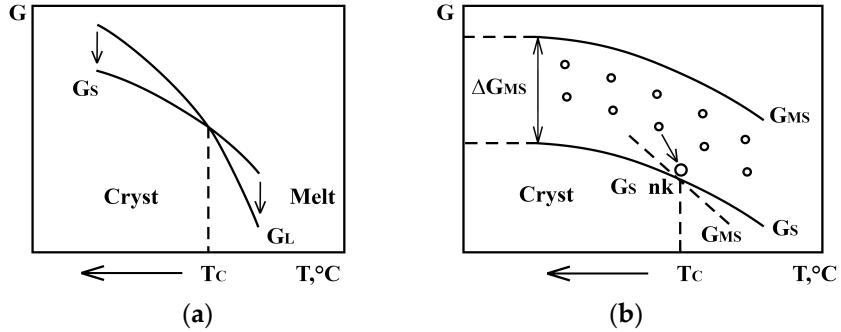

Figure 6. Temperature dependence of the Gibbs energy (for a crystallite with $G_S(T)$ energy) and (for a metastable phase with $G_{MS}(T)$ energy). Crystallization processes: (**a**) the arrow indicates the transition from the liquid phase (G_L) to the solid phase (G_S), the dotted line indicates the temperature of the phase transition (T_C); (**b**) the arrow indicates the transition from the metastable phase (ΔG_{MS}) to the solid phase. The point at which the G_{Snk} nucleus forms corresponds to the PT temperature T_c.

According to [26], the solubility of metastable phases exceeds the solubility of crystallites, so the slope angle in the G(T) plot of Figure 6b for the metastable phase G_{MS} will be larger than that for the solid phase G_{Snk} (shown by the dotted line). Crystallization must be accompanied by a decrease in the Gibbs energy by the value $\Delta G_{MS} < 0$, i.e., the following condition must be fulfilled:

$$\Delta G_{MS} = G_{MS} - G_S = \Delta H_s - T\Delta S_s, \quad (3)$$

where ΔH_S is the thermal effect of precursor transition from an amorphous to crystalline state. ΔS_S—the change in the entropy of the precursor because of the crystallization process.

Obviously, the G_{MS} energy and solubility (S_{MS}) of mobile activated particles are higher than the G_S energy and solubility (S_S) of crystallite nuclei, due to the condensation and dissolution of activated particles, i.e., after FT, the growth of nuclei to crystallites is possible. The grain growth model proposed in [31] may be suitable for this process. According to the classical atomistic theory [36], the grain boundary migration velocity (ν) can be written as follows [31]:

$$\nu = \lambda w_0 e\left(-\frac{\Delta G}{k_B T}\right)\left[1 - e\left(-\frac{\Delta G}{k_B T}\right)\right] \quad (4)$$

where ΔG is the activation energy; λ is the distance of each forward jump; w_0 is the frequency of atomic jumps; k_B is the Boltzmann constant; and T is the absolute temperature.

According to another model, the migration velocity of grain boundaries (v_{gb}) is determined as follows [32]:

$$v_{gb} = M_0 \exp\left(-\frac{E_a}{k_B T}\right) k\gamma \quad (5)$$

where M_0 is the entropic prefatory; E_a is the activation energy; a $k_B T$ is the thermal energy; k is the average grain boundary curvature; and γ is the grain boundary energy.

From the energy point of view, the grain boundary migration process can be represented as the FT (from amorphous phase to crystalline phase) $G_{MS} \rightarrow G_S$ using the energy ΔG_{MS}, which is given in Equation (1). Obviously, the process of grain boundary migration in type 2 samples will occur more easily (at lower activation energies) than in type 1 samples, since the crystallite growth rate in glass-phase precursors is higher (see Figure 4). Figure 7 schematically shows the FT processes of $G_{MS} \rightarrow G_S$ due to the activation energy of $E_a = \Delta G_{MS}$ in types 1 and 2 samples. Moreover, $\Delta G_{MS1} > \Delta G_{MS2}$.

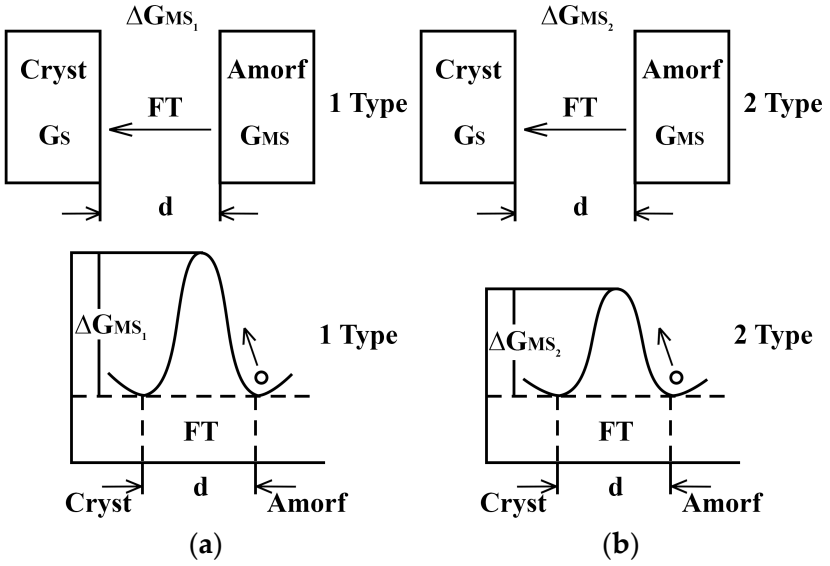

Figure 7. Schematic representation of the FP process from the amorphous phase to crystalline $G_{MS} \rightarrow G_S$ due to ΔG_{MS} energy: (**a**) for type 1 samples; (**b**) for type 2 samples. Moreover, $\Delta G_{MS2} > \Delta G_{MS1}$.

The data of the elemental compositions of the polycrystals are shown in Figure 8a,b and in Table 3.

Table 3. Elemental composition of $Na_3Fe_2(PO_4)_3$ polycrystals of type 1 and type 2 (Atom %).

Composition	Atom %	O	P	Fe	Na
Type 1 $Na_3Fe_2(PO_4)_3$	norm %	61.20	15.59	9.80	15.58
	fact %	61.24	15.60	9.10	15.60
	Off %	+0.04	+0.01	+0.02	+0.02
Type 2 $Na_3Fe_2(PO_4)_3$	norm %	59.02	14.51	10.02	16.48
	fact %	59.00	14.50	10.00	16.50
	Off %	−0.02	−0.01	−0.02	+0.02

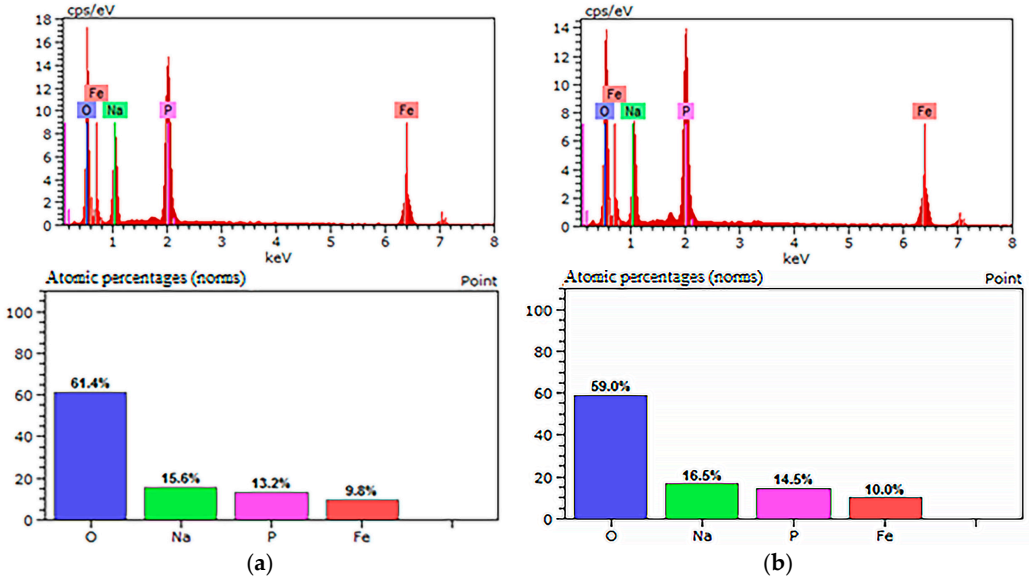

Figure 8. Elemental composition of $Na_3Fe_2(PO_4)_3$ polycrystals: (**a**) type 1 and (**b**) type 2.

The data on the elemental composition of both polycrystals show that there are insignificant deviations from the stoichiometric ratio of atoms. Losses of elements O, P, and Fe in the compositions of polycrystals of both types can be attributed to heat treatment during their synthesis. However, if the losses of these elements are hundredths of a per- cent, then the compositions of the samples can be considered stoichiometric (the diffractograms shown in Figure 1 indicate the single phase of both types of $Na_3Fe_2(PO_4)_3$ polycrystals).

Thus, the use of melt-quenching allows us to significantly accelerate the synthesis of $Na_3Fe_2(PO_4)_3$ polycrystals compared to the solid-phase method.

3.3. Ionic Conductivity of $Na_3Fe_2(PO_4)_3$ Polycrystals

The ionic conductivities of polycrystals of both types were measured (in the temperature range of 25–300 °C) using the impedance method [17]. For convenience in analyzing the conductive properties, the conductivity dependences σ(T) of the type 1 and 2 $Na_3Fe_2(PO_4)_3$ polycrystals in the α-, β-, and γ-phases are plotted in Figure 9. The conductivities of the polycrystals obey the Arrhenius laws.

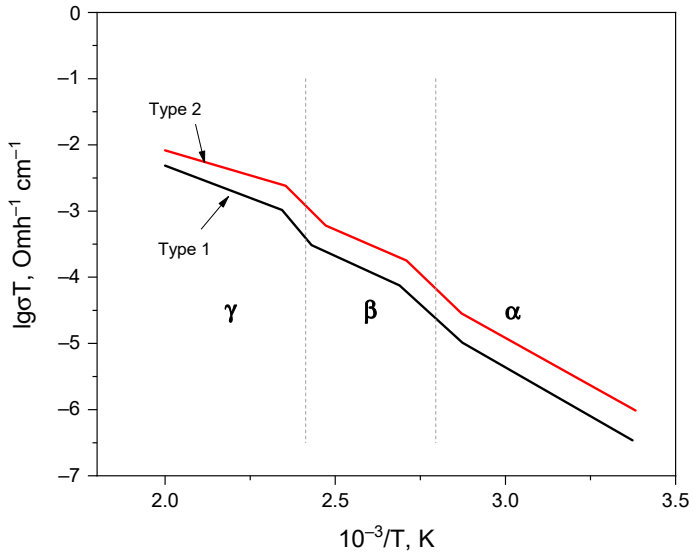

Figure 9. Temperature dependences of the ionic conductivity of $Na_3Fe_2(PO_4)_3$ for the type 1 (black line) and type 2 polycrystals (red line), α-, β-, and γ-phases are separated from each other by dotted lines.

Moreover, the σ(T) dependences of each phase are separated from each other by sloping steps at the points $T_{\alpha\to\beta}$ and $T_{\beta\to\gamma}$, located in the middle of the steps, since the FTs for polycrystals were not clearly manifested (see Figure 9). Using the σ(T) dependences of the type 1 and type 2 polycrystals, the conductivity parameters and PT temperatures of these samples were determined. The activation energies (ΔE) of the charge carriers of the samples in the α-, β-, and γ-phases were determined using graphs σ(T) (Figure 9) and Formula (6):

$$\Delta E = \frac{k\Delta \lg \sigma}{\Delta\left(\frac{1}{T}\right)} \quad (6)$$

where k is the Boltzmann constant and T is the absolute temperature.

Table 4 summarizes the ionic conductivity and FT temperatures for both types of $Na_3Fe_2(PO_4)_3$ polycrystals.

Table 4. Conductivity data and phase transition temperatures for the type 1 and 2 of $Na_3Fe_2(PO_4)_3$ polycrystals.

Parameters	Phases	Polycrystal $Na_3Fe_2(PO_4)_3$	
		1 Type	2 Type
Ionic conductivity σ, $(Om \cdot cm)^{-1}$	α (295 K)	3.8×10^{-7}	4.8×10^{-7}
	β (373 K)	5.6×10^{-5}	6.8×10^{-5}
	γ (573 K)	8.8×10^{-3}	10.0×10^{-3}
Activation energy ΔE, eV	α	0.63	0.61
	β	0.46	0.44
	γ	0.39	0.37
Temperatures of phase transitions: $T_{\alpha\to\beta}$, $T_{\beta\to\gamma}$, K		$T_{\alpha\to\beta}$ = 368	$T_{\alpha\to\beta}$ = 368
		$T_{\beta\to\gamma}$ = 418	$T_{\beta\to\gamma}$ = 418

The structures of both types of α-$Na_3Fe_2(PO_4)_3$ polycrystals are monoclinic-distorted, therefore characterized by low ionic conductivities and high activation energies (see Figure 9 and Table 4). These distortions of the anionic framework (α-$Na_3Fe_2(PO_4)_3$ led to the narrowing of the windows between the M(1) and M(2) cavities in the conduction channels of the crystal frameworks. Nevertheless, the conductivity of the type 2 α-$Na_3Fe_2(PO_4)_3$ polycrystal is higher and the activation energy values are slightly lower than in the type 1 sample. The reason for these changes in the type 2 samples may be the partial summarization of the crystal framework under the action of uniaxial deformation and the higher density caused by non-equilibrium thermodynamic conditions of synthesis. From the energetic point of view, the summarization of the structure is equivalent to a partial increase in the conduction window between the M(1) and M(2) cavities in the conduction channel.

The structures of the β-phase of the $Na_3Fe_2(PO_4)_3$ polycrystals are rhombohedral (pr. gr. 3RC) but possess the presence of small superstructural distortions of the crystal framework [19–22]. Hence, the conductivities of samples in this phase are lower and the activation energies are higher than in γ-$Na_3Fe_2(PO_4)_3$. After the β → γ phase transition, the structure becomes fully rhombohedral [20], so the conduction windows between the M(1) and M(2) cavities in the conduction channel are maximally open, and sodium cations are uniformly distributed in the cavities of the crystal framework. In γ-$Na_3Fe_2(PO_4)_3$, the mobility of sodium cations is high, and the potential barriers are reduced, so the ionic conductivity reaches maximum values in the presence of an external electric field.

Thus, the presence of structure deformation and the higher densities of the type 2 samples formed under non-equilibrium thermodynamic conditions of synthesis can partially lower the existing mechanical stresses in α-$Na_3Fe_2(PO_4)_3$, promoting greater openness in the "conduction window" for the movement of sodium cations in the conduction channel.

The deformation of the crystalline framework is confirmed by changes in the structural parameters (a, b, c and β) of the type 2 samples (see Table 2). It is likely that the higher conductivities of the type 2 samples in highly symmetric β- and γ-phases are related to a partial reduction in superstructural distortion under the action of uniaxial compression deformation. Also, questions about the relationship between crystal structure deformation and the ionic conductivity in α-$Na_3Fe_2(PO_4)_3$ were established in [18,21,22].

Based on the above, it follows that the structure and ion-conducting properties of $Na_3Fe_2(PO_4)_3$ polycrystals can be shaped by the choice of synthesis method. Due to the flexibility of the anionic crystalline framework $\{[Fe_2(PO_4)]^{3-}\}_{3\infty}$, $Na_3Fe_2(PO_4)_3$ polycrystals of different degrees of structure deformation can be formed depending on the thermodynamic conditions of synthesis. Using melt-quenching to obtain $Na_3Fe_2(PO_4)_3$ polycrystals makes it possible to form, in their structure, high-quality crystallites with higher conductivities than in samples obtained by solid-phase synthesis.

The melt-hardening method of obtaining polycrystals used in this work shows practical efficiency, i.e., this technology allows high-quality samples to be synthesized, accelerates the crystallization process, and is simple in terms of technological execution. In the future, the use of melt-quenching in the synthesis of cathode materials could contribute to an increase in the energy parameters in SIB, so this method of synthesis deserves attention and further improvement.

4. Conclusions

According to the results of this study of type 1 and type 2 $Na_3Fe_2(PO_4)_3$ polycrystals, we can conclude the following:

(1) Polycrystals (type 2) are better obtained by melt-quenching because the solid-phase crystallization of the crystallites in them occurs better and faster than in samples (type 1) prepared by solid-phase synthesis.

(2) The type 2 α-$Na_3Fe_2(PO_4)_3$ polycrystals formed from glassy precursors consist mainly of small to medium-sized crystallites and are denser than type 1 polycrystals. The probable cause of the higher conductivity of type 2 α-$Na_3Fe_2(PO_4)_3$ polycrystals compared to type 1 samples is the uniaxial compression deformation of the structure, which can partially reduce the existing monoclinic distortions in their structure. The higher conductivities of type 2 samples in the β- and γ-phases are associated with a partial reduction in superstructural distortion under the action of the residual compressive deformation of the sample, as well as an increase in their density.

(3) The advantage of using melt-quenching to obtain $Na_3Fe_2(PO_4)_3$ polycrystals is that the method is simple, less energy-consuming and significantly reduces the number of times that synthesis is performed (four times) compared to the ceramic method. This method can be effective in obtaining ionic conductors with other compositions to improve their conductive properties.

Author Contributions: Conceptualization, A.S.N.; methodology, D.E.U., software, B.A.-D.B. and A.A.A.; validation, P.A.D. and A.S.T.; formal analysis, A.B.U.; investigation, E.A.N. and A.A.N.; resources and data curation, D.E.U.; writing—original draft preparation, A.A.N.; writing—review and editing, A.S.N.; project administration, and funding acquisition, A.S.N. All authors have read and agreed to the published version of the manuscript.

Funding: This research was funded by the Ministry of Science and Higher Education of the Republic of Kazakhstan, grant number: AP14871881.

Data Availability Statement: The necessary data is provided in the article.

Conflicts of Interest: The authors declare no conflicts of interest.

References

1. Tan, K.M.; Babu, T.S.; Ramachandaramurthy, V.K.; Kasinathan, P.; Solanki, S.G.; Raveendran, S.K. Empowering smart grid: A comprehensive review of energy storage technology and application with renewable energy integration. *J. Energy Storage* **2021**, *39*, 102591. [CrossRef]
2. Amir, M.; Deshmukh, R.G.; Khalid, H.M.; Said, Z.; Raza, A.; Muyeen, S.; Nizami, A.-S.; Elavarasan, R.M.; Saidur, R.; Sopian, K. Energy storage technologies: An integrated survey of developments, global economical/environmental effects, optimal scheduling model, and sustainable adaption policies. *J. Energy Storage* **2023**, *72*, 108694. [CrossRef]
3. Worku, M.Y. Recent Advances in Energy Storage Systems for Renewable Source Grid Integration: A Comprehensive Review. *Sustainability* **2022**, *14*, 5985. [CrossRef]
4. Chen, Y.; Kang, Y.; Zhao, Y.; Wang, L.; Liu, J.; Li, Y.; Liang, Z.; He, X.; Li, X.; Tavajohi, N.; et al. A Review of lithium-ion battery safety concerns: The issues, strategies, and testing standards. *J. Energy Chem.* **2021**, *59*, 83–99. [CrossRef]
5. Bauer, A.; Song, J.; Vail, S.; Pan, W. The Scale-up and Commercialization of Nonaqueous Na-Ion Battery Technologies. *Adv. Energy Mater.* **2018**, *8*, 1702869. [CrossRef]
6. Niu, Y.; Zhang, Y.; Xu, M.-W. A Review on Pyrophosphates Framework Cathode Materials for Sodium-ion Batteries. *J. Mater. Chem. A* **2019**, *7*, 15006. [CrossRef]
7. Yabuuchi, N.; Komaba, S. Recent research progress on iron- and manganese-based positive electrode materials for rechargeable sodium batteries. *Sci. Technol. Adv. Mater.* **2014**, *4*, 043501. [CrossRef]
8. Kanwade, A.; Gupta, S.; Kankane, A.; Srivastava, A. Phosphate-based cathode materials to boost the electrochemical performance of sodium-ion batteries. *Sustain. Energy Fuels* **2022**, *6*, 3114–3147. [CrossRef]
9. Kalinin, V.B.; Stefanovich, S.Y.; Nogai, A. Crystal chemistry and properties of compounds with rhombohedral frameworks of the composition $\{[M_2(TO_4)_3]^{3-}\}_{3\infty}$. and solid solutions based on them. *Inorg. Mater.* **1986**, *22*, 107–111.
10. Wang, J.; He, T.; Yang, X.; Cai, Z.; Wang, Y.; Lacivita, V.; Kim, H.; Ouyang, B.; Ceder, G. Design principles for NASICON super-ionic conductors. *Nat. Commun.* **2023**, *14*, 5210. [CrossRef]
11. Efremov, V.A.; Kalinin, V.B. Determination of the crystal structure of $Na_3Sc_2(PO_4)_3$. *Crystallography* **1978**, *20*, 703–708.
12. Ouyang, B.; Wang, J.; He, T.; Bartel, C.J.; Huo, H.; Wang, Y.; Lacivita, V.; Kim, H.; Ceder, G. Synthetic accessibility and stability rules of NASICONs. *Nat. Commun.* **2021**, *12*, 5752. [CrossRef] [PubMed]
13. Nogai, A.S.; Nogai, A.A.; Stefanovich, S.Y.; Solikhodzha, Z.M.; Uskenbaev, D.E. Dipole ordering and ionic conductivity in NASICON-like structures such as $Na_3Sc_2(PO_4)_3$. *Phys. Solid State* **2019**, *61*, 2016–2023. [CrossRef]
14. Sorokin, N.I. Na^+-ion conductivity of double phosphate $Na_3Sc_2(PO_4)_3$ in the region of the γ-β transition. *Phys. Solid State* **2014**, *56*, 678–681. [CrossRef]
15. Rettenwander, D.; Redhammer, G.J.; Guin, M.; Benisek, A.; Krüger, H.; Guillon, O.; Wilkening, M.; Tietz, F.; Fleig, J. Arrhenius Behavior of the Bulk Na-Ion Conductivity in $Na_3Sc_2(PO_4)_3$ Single Crystals Observed by Microcontact Impedance Spectroscopy. *Chem. Mater.* **2018**, *30*, 1776–1781. [CrossRef]
16. Ladenstein, L.; Lunghammer, S.; Wang, E.Y.; Miara, L.J. On the dependence of ionic transport on crystal orientation in NASICON–type solid electrolytes. *J. Phys. Energy* **2020**, *2*, 035003–035009. [CrossRef]
17. Nogai, A.S.; Nogai, A.A.; Stefanovich, S.Y.; Solikhodzha, Z.M.; Uskenbaev, D.E. Dipole Ordering and Ionic Conductivity in NASICON-Like Structures of the $Na_3Fe_2(PO_4)_3$ Type. *Phys. Solid State* **2020**, *62*, 1370–1379. [CrossRef]
18. Nogai, A.A.; Salikhodzha, Z.M.; Nogai, A.S.; Uskenbaev, D.E. Conducting and dielectric properties of $Na_3Fe_2(PO_4)_3$ and Na_2FePO_4F. *Eurasian J. Phys. Funct. Mater.* **2021**, *5*, 222–234. [CrossRef]
19. D'Yvoire, F.; Pintard-Screpel, M.; Bretey, E.; de la Rochère, M. Phase transitions and ionic conduction in 3D skeleton phosphates $A_3M_2(PO_4)_3$: A = Li, Na, Ag, K.; M = Cr, Fe. *Solid State Ion.* **1983**, *9–10*, 851–858. [CrossRef]
20. Pintard–Screpel, M.; D'Yvoire, F.; Remy, E. Polimorphisme et conduction ionique du phosphate $Na_4Fe_2(PO_4)_3$. *C. R. Acad. Sci.* **1978**, *286*, 381–383.
21. Kravchenko, V.V.; Sigaryov, S.E. Structural features of the superionic phase transitions in $Na_3Fe_2(PO_4)_3$. *Solid State Commun.* **1992**, *83*, 149–152. [CrossRef]
22. Lyubutin, I.; Melnikov, O.; Sigaryov, S.; Terziev, V. Phase transitions in $Na_3Fe_2(PO_4)_3$. *Solid State Ion.* **1988**, *31*, 197–201. [CrossRef]
23. Masquelier, C.; Wurm, C.; Rodríguez-Carvajal, J.; Gaubicher, J.; Nazar, L. A Powder Neutron Diffraction Investigation of the Two Rhombohedral NASICON Analogues: γ-$Na_3Fe_2(PO_4)_3$ and $Li_3Fe_2(PO_4)_3$. *Chem. Mater.* **2000**, *12*, 525–532. [CrossRef]
24. Liu, Y.; Zhou, Y.; Zhang, J.; Xia, Y.; Chen, T.; Zhang, S. Monoclinic phase $Na_3Fe_2(PO_4)_3$: Synthesis, structure, and electrochemical performance as cathode material in sodium-ion batteries. *ACS Sustain. Chem. Eng.* **2016**, *5*, 1306–1314. [CrossRef]
25. Nogai, A.S.; Nogai, A.A.; Nogai, E.A.; Bush, A.A.; Uskenbaev, D.E. Influence of substitutions on the structure ionic conductivity and phase transition in the system of $Na_3Fe_{2(1-x)}Sc_{2x}(PO_4)_3$ ($0 \leq x \leq 0.06$) solid solutions. *Eurasian J. Phys. Funct. Mater.* **2023**, *7*, 107–114. [CrossRef]
26. Nogai, A.S.; Uskenbaev, D.E.; Utegulov, A.B.; Nogai, E.A.; Toleugulov, D.D. Features of Structures and Ionic Conductivity of $Na_3Fe_2(PO_4)_3$ Polycrystals Obtained by Solid Phase and Mellte Methods. *Ceramics* **2023**, *6*, 2295–2306. [CrossRef]
27. He, Y.; Li, H. Recent Research Process of Carbon Engineering on $Na_3V_2(PO_4)_3$ for Sodium-Ion Battery Cathodes: A Mini Review. *Electron. Mater.* **2023**, *4*, 17–32. [CrossRef]
28. Wu, X.; Zhong, G.; Yang, Y. Sol–gel synthesis of $Na_4Fe_3(PO_4)_2(P_2O_7)$/C nanocomposite for sodium ion batteries and new insights into microstructural evolution during sodium extraction. *J. Power Sources* **2016**, *327*, 666–674. [CrossRef]

29. Cao, Y.; Liu, Y.; Chen, T.; Xia, X.; Zhang, L.-C.; Zhang, J.; Xia, Y. Sol-gel synthesis of porous $Na_3Fe_2(PO_4)_3$ with enhanced sodium-ion storage capability. *Ionics* **2019**, *25*, 1083–1090. [CrossRef]
30. Sun, W.; Ceder, G. Induction time of a polymorphic transformation. *Cryst.Eng.Comm.* **2017**, *19*, 4576–4585. [CrossRef]
31. Hu, J.; Wang, X.; Luo, J.; Zhang, Z.; Shen, Z. A general mechanism of grain growth—I. *Theory J. Mater.* **2021**, *7*, 1007–1013.
32. Rohrer, G.S.; Chesser, I.; Krause, A.R.; Naghibzadeh, S.K.; Dayal, K.; Holm, E.A. Grain Boundary Migration in Polycrystals. *Annu. Rev. Mater. Res.* **2023**, *53*, 347–369. [CrossRef]
33. Nitsche, H.; Stanislowski, M.; Sommer, F.; Mittemeijer, E.J. Kinetics of crystallization of amorphous $Mg_{80}Cu_{10}Y_{10}$. *Z. Met.* **2005**, *96*, 1341–1350. [CrossRef]
34. Shen, Z.; Zhao, Z.; Peng, H.; Nygren, M. Formation of tough inter locking microstructures in silicon nitride ceramics by dynamic ripening. *Nature* **2002**, *417*, 266–269. [CrossRef] [PubMed]
35. Kang, S.-J.L.; Lee, M.-G.; An, S.-M. Microstructural evolution during sintering with control of the interface structure. *J. Am. Ceram. Soc.* **2009**, *92*, 1464–1471. [CrossRef]
36. Adland, A.; Xu, Y.; Karma, A. Unified theoretical framework for polycrystalline pattern evolution. *Phys. Rev. Lett.* **2013**, *110*, 265504. [CrossRef]
37. Ovid'ko, I.A. Theories of Grain Growth and Methods of Its Suppression in Nanocrystalline and Polycrystalline Materials. *Mater. Phys. Mech.* **2009**, *8*, 174–199.
38. Mishra, S.; DebRoy, T. Non-isothermal grain growth in metals and alloys. *Mater. Sci. Technol.* **2006**, *22*, 253–278. [CrossRef]